26

Exploring the Superconductors with Scanning Electron Microscopy (SEM)

Shiva Kumar Singh[1,2,*], Devina Sharma[1], M. Husain[2], H. Kishan[1], Ranjan Kumar[3] and V.P.S. Awana[1]

[1]*Quantum Phenomena and Applications, National Physical Laboratory (CSIR), New Delhi,*

[2]*Department of Physics, Jamia Millia Islamia, New Delhi,*

[3]*Department of Physics, Panjab University, Chandigrah, India*

1. Introduction

The characterization of materials supports their development and in particular of superconductors, for their technological applications. Scanning electron microscopy (SEM) is one of these characterization techniques, whose data is used to estimate the properties, determine the shortcomings and hence improve the material. The phenomenon of superconductivity initially develops within the grain and eventually crosses over the grain boundaries, leading to the bulk. Hence SEM can be a useful tool to probe the microstructure of the superconductors and the properties related to it. Along with this the Energy-dispersive Spectroscopy (EDS) can tell about the chemical composition of compounds. Grain size and its connectivity can be seen through SEM and can be correlated with the corresponding properties. The superconducting materials developed for practical applications are some of the complex materials used today. These materials have large number of potential variables such as their processing conditions, composition, structure etc., whose dependence on the superconducting properties have to be analyzed critically. The characterization techniques are the tools that help to reveal and explore both the macro and microstructure of materials. It is known that the larger grains (reduction in grain boundaries) lead to increased pinning type behavior with enhanced J_c [1]. In contrast Rosko *et al.* [2] reported that J_c is determined by weak links and grain size has little role on it. Also, Smith *et al.* [3] interpreted reduction of J_c and activation of weak link type behavior with increasing grain size for $YBa_2Cu_3O_{7-\delta}$ (YBCO) polycrystalline samples in terms of micro-cracks in large grains. The superconducting parameters are broadly divided into two categories; first, the intrinsic parameters such as penetration depth (λ), which are intrinsic to the material and are not affected by, grain size. On the other hand, values such as shielding/Meissner fraction, the inter- and intra-grain critical current density and diamagnetic fraction depend upon particle size of bulk superconductors. Thus SEM can be very important to probe and in understanding the superconducting phenomena.

* Corresponding Author

In SEM electron beam is scanned across a sample's surface. When the electrons strike the sample, a verity of signals arises and produces elemental composition of the sample. *SEM* with *EDS* is a major tool for qualitative and quantitative analyses which is done by bombarding a finely focused electron beam (electron probe) on the specimen, and measuring the intensities of the characteristic X-ray emitted. The three signals in SEM are the secondary electrons, backscattered electrons and X-rays, provide the greatest amounts of information. Secondary electrons are emitted from the atoms occupying the top surface and produce interpretable image of the surface. The contrast in the image is determined by the sample morphology. Backscattered electrons are primary electrons which are "reflected" from atoms in the solid. The contrast in the image produced is determinate by the atomic numbers of the elements in the sample. Therefore the image shows the distribution of different chemical elements in the sample. Since these electrons are emitted from the depth of the sample, the resolution of the image is not as good as for secondary electrons.

This chapter deals with the ability of SEM in extracting the information from superconductors. Since, the microstructure and topology of the materials determine largely its properties in terms of its grains and their connectivity, the utility of SEM in studying the properties of various superconductors discovered till date will be reviewed. The limitations will also be discussed. How other characterization tools, can provide better information along with *SEM*, will be explored.

2. SEM: As a characterization tool for superconductors

Some of the important aspects with which *SEM* deals with, is the grain size, morphology and alignment, structural defects, chemical composition. While trying to optimize the transport properties, grain to grain alignment within the superconductor has to be considered. It is important to analyze the grain alignment and enhance it in order to relate it to the improvement of transport properties. Defects play an important role in determining the properties of superconductors, especially those of HTSc. While macro defects such as porosity, cracks, secondary phases etc. may adversely affect the transport critical super currents, on the other hand microscopic defects such as addition of nanoparticles, dislocation etc., can prove to be beneficial. As the size of the defects is smaller than the coherence length of the superconductor, they may act as pinning centers, thereby enhancing the critical current. Chemical composition of the material within the superconducting grain and at the grain boundaries has significant effect over its properties. The compositions and the change in the compositions can be measured or inferred from a variety of techniques such as energy dispersive spectroscopy. Backscattered electron imaging (BEI) can also be used to infer chemical compositional variations. In all, the complexity in the superconducting materials requires continuous research into their fundamental properties and evolution of new improved materials. For all these evaluations, various characterization tools have to be relied upon among which SEM and allied techniques such as EDS and BEI play an important role.

2.1 Determination of grain size from *SEM* micrographs

Grain size determination is perhaps one of the most commonly performed microstructural measurements from *SEM* micrographs. Standards organizations, including American Society for Testing and Materials (ASTM) [4] and some other national and international

organizations, have developed standard test methods describing how to characterize microstructures quantitatively. The methods for grain size measurement are described in great detail in the ASTM Standard, E112, "Standard Test Methods for Determining Average Grain Size" [5]. The information below will provide cursory explanation to the methods for determining grain size in *ASTM* E112. The microstructural quantity known as the *ASTM* micro gain size number, G is defined as

$$n = 2^{G-1}$$

Where, n is the number of grains per square inch measured at a magnification of 100x. Grain size or the value of G is most commonly measured by (a) Planimetric method and by (b) Intercept method.

(a) Planimetric method

In the Planimetric method [Fig. 1 (a)] (developed by Zay Jeffries in 1916), a count is made of the number of grains completely within a circle of known area and half of the number of grains intersected by the circle to obtain N_A. Then, N_A is related to G. This method is slow when done manually because the grains must be marked when counted to obtain an accurate count. This method is described in the section 9 of *ASTM E112*.

The basic steps of the procedure are as follows:

i. A circle of known size is inscribed over the SEM image.
ii. The numbers of grains are counted that are completely within the area (n_{inside}).
iii. The number of grains is counted that are partially within the area ($n_{intercepted}$).
iv. The number of grains per sq. mm, N_A, is calculated from $N_A = f \{n_{inside} + ½(n_{intercepted})\}$
v. The multiplier f is calculated from (M^2/circle area), where M is the linear magnification of the image.
vi. From N_A, we can calculate the *ASTM* grain size number, G, using the following formula from E 112-96:$G = \{3.322 (\log10\ N_A) – 2.954\}$

(b) Linear intercept method

The *ASTM* grain size can also be determined using the intercept method (developed by Emil Heyn in 1904) counting either the number of grains intercepted (N) or the number of grain boundaries intersected (P) with a test line. *ASTM* recommends using a grid with three concentric circles (as shown in the Fig. 1 (b)) with a 500mm total line length. The count of the number of grains intercepted by the circle is N. To calculate the number of interceptions per mm, N_L, we divide N by the true length of the circle. The true length (L_T) is obtained by dividing the circumference of the circle by the magnification, M. Hence, $N_L = N/L_T$ interceptions per mm. To calculate the grain size, we first determine the mean linear intercept length, *l*, which is the reciprocal of N_L (or of P_L, the number of grain boundary intersections per unit length). G is calculated from an equation from E 112-96:

$$G = \{-6.644 (\log10\ l) – 3.288\},$$

where, *l* is in mm.

ASTM E112 provides table that relates grains/in^2 @ 100x and grains/mm^2 @ 1x to *ASTM* grain size number G. Since the two methods are sensing different geometric aspects of the

three-dimensional grain structure, they will not give exactly the same value, but they will be close, generally within the experimental limitations of the measurements. In practice, these measurements are repeated on a number of fields in order to obtain a good estimate of the grain size.

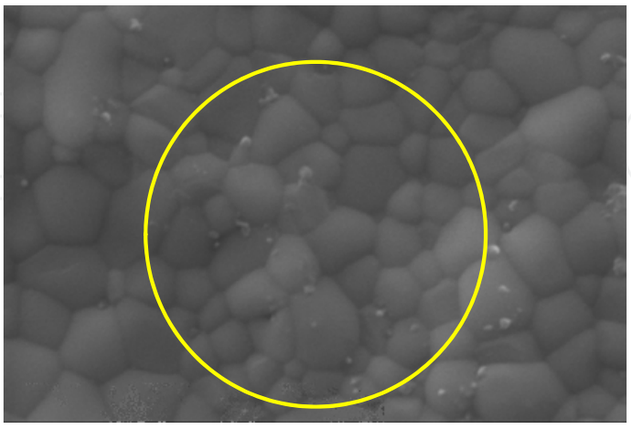

(a)

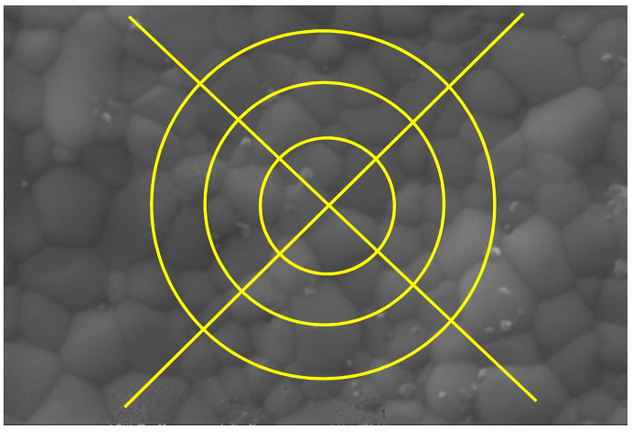

(b)

Fig. 1. **(a)** Planimetric method, **(b)** Linear Intercept method

2.2 Chemical composition using EDS

One of the most outstanding features of the *SEM-EDS* is that it allows elemental analysis and observation from an ultra micro area to a wide area on the specimen surface without destroying the specimen. Qualitative and quantitative analysis (by *EDS*) by electron probe takes advantage of the emission of characteristic X-radiation by electron interactions in the valence shell of atoms. Backscattered electron images in the *SEM* display compositional contrast that results from different atomic number and their distribution of elements. *EDS* allows one to identify what those particular elements are and their relative proportions, for example their atomic percentage. Initial EDS analysis usually involves the generation of an X-ray spectrum from the entire scan area of the SEM. In the X ray spectra generated from the entire scan, Y-axis shows the counts (number of X-rays received and processed by the

detector) and the X-axis shows the energy level of those counts. The EDS software associates the energy level of the X-rays with the elements and shell levels that generated them.

3. Exploring superconductors using *SEM*

In this section we will discuss the *SEM* study of superconductors of different families. For high temperature superconductors (HTSc), *SEM* has been widely used to explore the superconducting behavior. Grain size matters a lot in deciding the superconducting parameters of cuprate HTSc. Decrease in shielding current is observed with decrease in particle size [6]. Magnesium diboride (MgB_2) represent an attractive alternative to low temperature superconductors. For most of the practical applications, high critical current density (J_c) in the presence of a magnetic field along with high upper critical field (H_{C2}) and high irreversibility field (H_{irr}) are required. Moderate impurities and nano (n) materials are being used to improve these parameters [7-14]. In particular, significant flux pinning enhancement in MgB_2 is observed with *n-SiC* addition [15]. In case of newly discovered pnictides superconductors, *SEM* is being used in an ingenious way. The spatially resolved electrical transport properties have been studied on the surface of optimally-doped superconducting $Ba(Fe_{1-x}Co_x)_2As_2$ single crystal by using a four-probe scanning tunneling microscopy [16]. Results will be discussed in following subtitles.

3.1 Grain size and gain connectivity in cuprate high temperature superconductors

One of the characteristics of high temperature superconductors (HTSc) is their small coherence length which is comparable with the unit cell. The coherence length is a key parameter for the performance of superconductors for applications, since this determines the size of the normally conducting core of the flux lines [17]. In order to control the motion of flux lines one needs a microstructure with defects as small as the coherence length. The extremely small coherence length of HTSc, which is for YBCO only 2.7 nm at 77 K within the ab-plane, is the reason that defects such as grain boundaries, which are very beneficial in low-temperature superconductors because they act as pinning defects, serve as weak links and limit the critical current, especially in the presence of an external magnetic field. HTSc bulk material can therefore be considered as a matrix of superconducting grains embedded in a non superconducting material.

The cuprate superconductors belong to the family of HTSc in which Cu-O chains and planes are responsible for the conduction of super currents. The size as well as the shape of the grains varies in different cuprate HTSc [18-20]. This variation in microstructure in turn leads to different superconducting behavior. Although the nature of the occurrence of superconductivity in cuprate HTSc is same, T_c varies from 38 K in LSCO to 110 K in BSCCO system. This wide range of T_c itself indicates that micro-structural parameters are of much importance. In this section various cuprate HTSc will be discussed in the chronological order of their discovery, in terms of the use of SEM for their characterization.

A. $La_{2-x}Sr_xC_uO_4$

Discovered by Bednorz and Muller in 1986 [21], $La_{2-x}Sr_xCuO_4$ was the trendsetter breakthrough in the history of superconductivity leading to the new era of High T_c superconductivity. It has T_c of 38 K which is beyond the BCS limit of 30 K. Although it has

higher T_c than conventional superconductors, its critical parameters such as critical temperature, field and current density, which are applicable in practical applications, are weaker. Various attempts had been made earlier to enhance these parameters and to understand the physics behind it. The values such as shielding/Meissner fraction, the inter- and intra-grain critical current density and diamagnetization fraction depends upon particle size of bulk superconductors. One of the earliest reports on the effect of particle size on the physical properties of a superconductor was by Chiang et al. [22], who varied particle size from 1 to 10 μm and found significant changes in the superconducting and physical properties. Another fact that has well been established is that the critical current measurements done in HTSc have shown a much lower value for polycrystalline bulk samples [1] than single crystals of the same compound. This difference cannot be attributed alone to the intrinsic nature (anisotropy etc.) of the material. In fact, the quasi-insulating grain boundaries of HTSc play a detrimental role in limiting the critical current and other superconducting and magnetic properties [22-23]. In a recent report D. Sharma et al. [18] have investigated the influence of grain size (sintering temperature) on various superconducting parameters in $La_{1.85}Sr_{0.15}CuO_4$. From SEM micrographs [see Fig. 2 (a), (b) and (c)] it is clear that with the increase in the sintering temperature, there is a considerable increase in the grain size. Increment in the grain size brings in double boom to the superconductivity as it reduces the number of insulating grain boundaries (weak links) as well as increases the effective superconducting volume fraction. Thus both the inter and intra critical current density which is limited by the weak links is expected to enhance with increase in the grain size. Qualitative picture given by the SEM micrographs corroborates with the quantitative results obtained from various transport and magnetic measurements as given in the table 1.

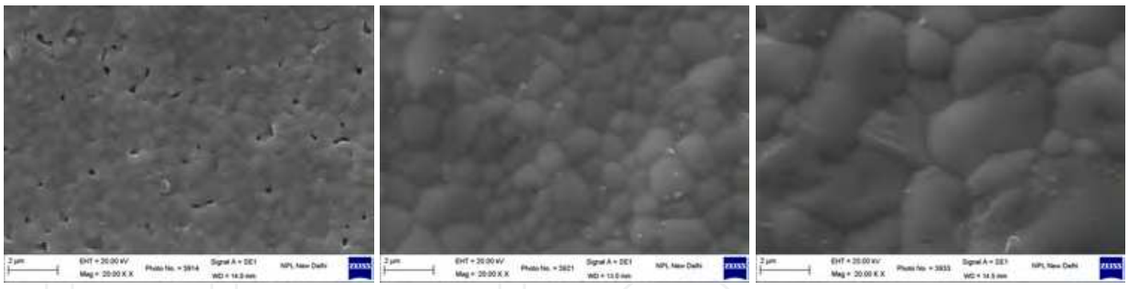

Fig. 2. SEM of $La_{1.85}Sr_{0.15}CuO_4$ samples sintered at (**a**) 900 °C, (**b**) 1000 °C, and (**c**) 1050 °C [Ref. 18].

Grain size ($2R$)	Critical current density J_c (A/cm^2)		Diamagnetization (at $T = 10$ K, $H = 10$ Oe)		Volume fraction not penetrated $(R-\lambda)^3/R^3$
	$J_c = (20 \times \Delta M)/a(1 - a/3b)$ Inter-granular J_c	$J_c = (15 \times \Delta M \times \rho)/R$ Intra-granular J_c	ZFC	FC	
1 μm	1.1×10^3	3.75×10^5	0.36%	0.28%	9.08%
2 μm	3.8×10^3	8.36×10^5	2.10%	1.59%	38.07%
4.5 μm	40.4×10^3	32.73×10^5	16.95%	4.08%	64.20%

Table 1. Critical current density, diamagnetization fraction and percentage volume fraction not penetrated by magnetic flux calculated from magnetic measurement data for different grain sizes of $La_{1.85}Sr_{0.15}CuO_4$ [Ref. 18].

In another particle size controlled study of non-superconducting $La_{1.96}Sr_{0.04}CuO_4$ was made with SEM and IR spectra by S. Zhou et al [24]. They observed that as the particle size reduces, the IR band at around 685 cm^{-1}, corresponding to in-plane Cu–O asymmetrical stretching mode, shifts to higher frequency and the magnetization exhibits a large enhancement at low temperature. A visible spin-glass transition was found under a relatively weak external field in the sample with the largest particle sizes. Whereas the sample with the smallest particle sizes exhibits no visible spin-glass transition. They suggested that surface effects play a dominant role in determining the magnetic properties as the particle size reduces.

B. $YBa_2Cu_3O_{7-\delta}$

Cuprate superconductors are very sensitive to oxygen content. Depending on oxygen content, $YBa_2Cu_3O_{7-\delta}$ crystallizes in two phases. Tetragonal *P4/mmm* with $\delta = 0.60$ results in non-superconducting and antiferromagnetic YBCO whereas orthorhombic *pmmm* with $\delta = 0.05$ phase leads to a superconducting YBCO with T_c 93 K [25]. Also, the intra-grain signal depends much on oxygen content of the composition. The structure of YBCO can be viewed as (Ba,Sr)O/CuO_2/RE/CuO_2/(Ba,Sr)O slabs interconnected through a sheet of Cu and O with variable composition of CuO_x.. Charge transport and high temperature superconductivity is believed to reside in the CuO_2 planes of all known HTSc cuprates, except that $CuO_{1+\delta}$ chains have been reported to participate in the *b*-axis transport of $YBa_2Cu_3O_{7-\delta}$ [26]. In $YBa_2Cu_3O_{7-\delta}$ ($CuBa_2YCu_2O_{7-\delta}$, Cu-1212) there are two different Cu sites, namely Cu1 and Cu2. Cu1 resides in CuO_x chains and Cu2 in superconducting CuO_2 planes. Even at macroscopic level, any contravene in integral CuO_2 stacks, affects superconductivity drastically [27-28]. The CuO_x chain acts as a charge reservoir and provides the mobile carriers to superconducting CuO_2 planes.

To understand the physics of the superconducting nature, investigation of doping various elements at Cu1 site was carried by some of us [29]. And it was found that the YBCO structure is versatile and changes with doped elements at Cu1 site. Single phase samples of 1212 type with different MOx layers showed the great flexibility of these rocksalt layers and variable structure formation. With different M, as the oxidation state and ionic state changes, carrier concentration and structure changes as well. While, Nb-, Fe-, Ru- and Al-1212 possess tetragonal *P4/mmm* space group structure, the Ga-1212 and Co-1212 are crystallized in orthorhombic *Ima2* space group.

The SEM images [Fig. 3] suggest that with the doping of variety of elements at the Cu1 site in Y-123 structure, the morphology also changes suggesting change in the structure of the new compounds formed. Change in structure was authenticated by the Rietveld analysis also. In another report Nalin *et al.* [30] studied effect of Zn doping at Cu1 site. With ac susceptibility inter and intra granular changes are studied. In the Zn-doped samples, the inter-grain peak got reduced dramatically. In the χ^{II} plots of Zn doped samples the inter-grain peak superposes with intra-grain peak and inter-grain peak depresses further. It was concluded that as (see *SEM* images [Fig. 4]) the average grain size is increasing with Zn doping. The increased grain size provides more area for the eddy currents loops to persist in the individual grains, thus systematic enhancing the intra-grain peak.

A combined study through *SEM* and *EDS* for the compounds $Y_{1-x}Ca_xBa_{1.9}Nd_{0.1}Cu_3Oy$ (YCBNCO) with $x \leq 0.40$ have been made [31]. Back-scattered electron SEM micrographs of samples with $x = 0.10$ and 0.30 have been taken. The *SEM* studies proved that the samples

with x ≤ 0.20 are homogeneous and stone like grains with typical size of several microns. On the other hand the samples with x ≥ 0.20 are inhomogeneous. The *SEM* micrographs show that the stone-like grains and the sponge-like grains co-exist in the surface of the samples. The *EDS* results show that the constituted elemental ratios in both regions are different and hence the superconducting properties.

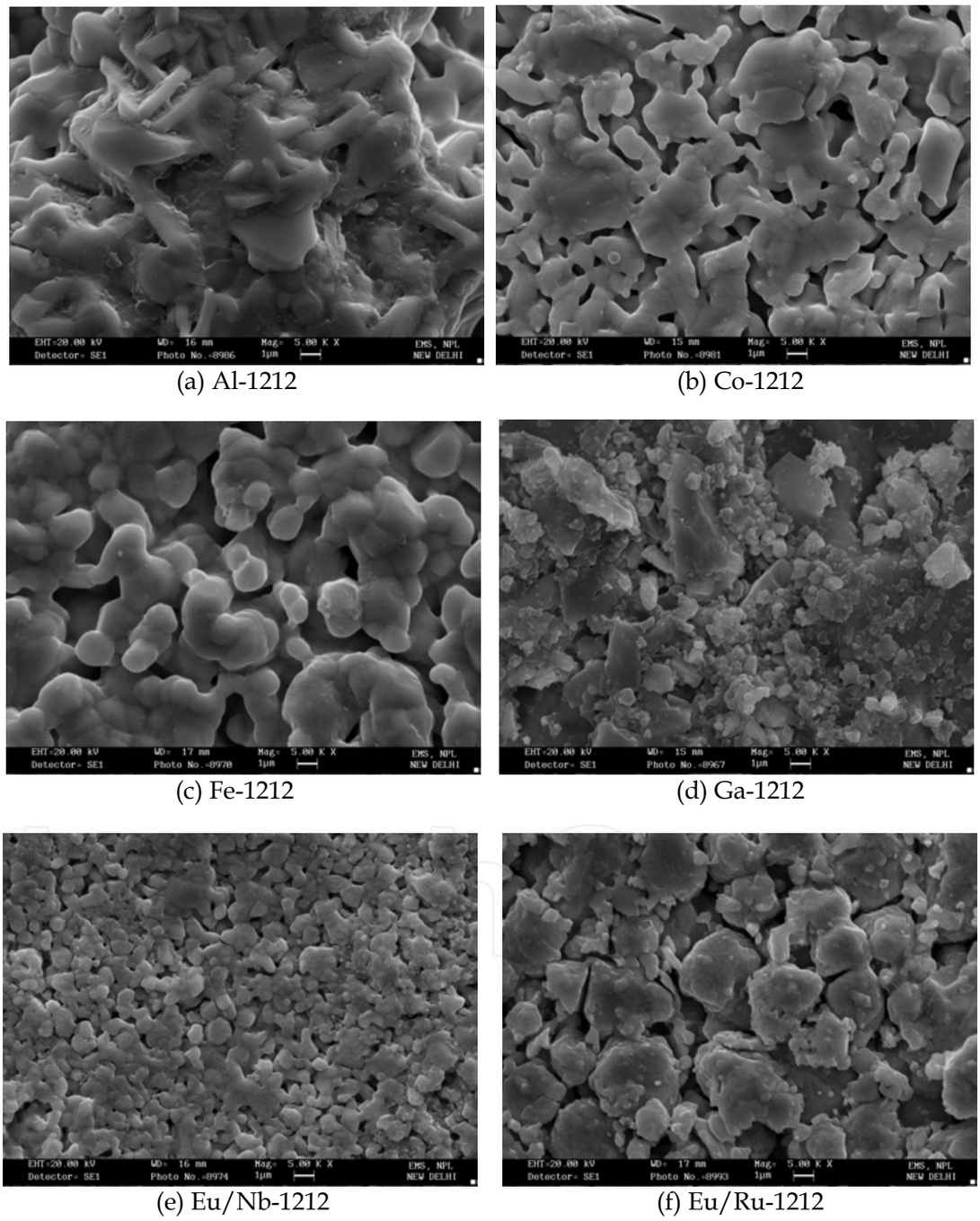

(a) Al-1212 (b) Co-1212

(c) Fe-1212 (d) Ga-1212

(e) Eu/Nb-1212 (f) Eu/Ru-1212

Fig. 3. SEM pictures of the M-1212: (a) $AlSr_2YCu_2O_{7+\delta}$, (b) $CoSr_2YCu_2O_7$, (c) $FeSr_2YCu_2O_{7+\delta}$, (d) $GaSr_2YCu_2O_7$, (e) $NbSr_2EuCu_2O_{7+\delta}$ and (f) $RuSr_2EuCu_2O_{7+\delta}$. [Ref. 29].

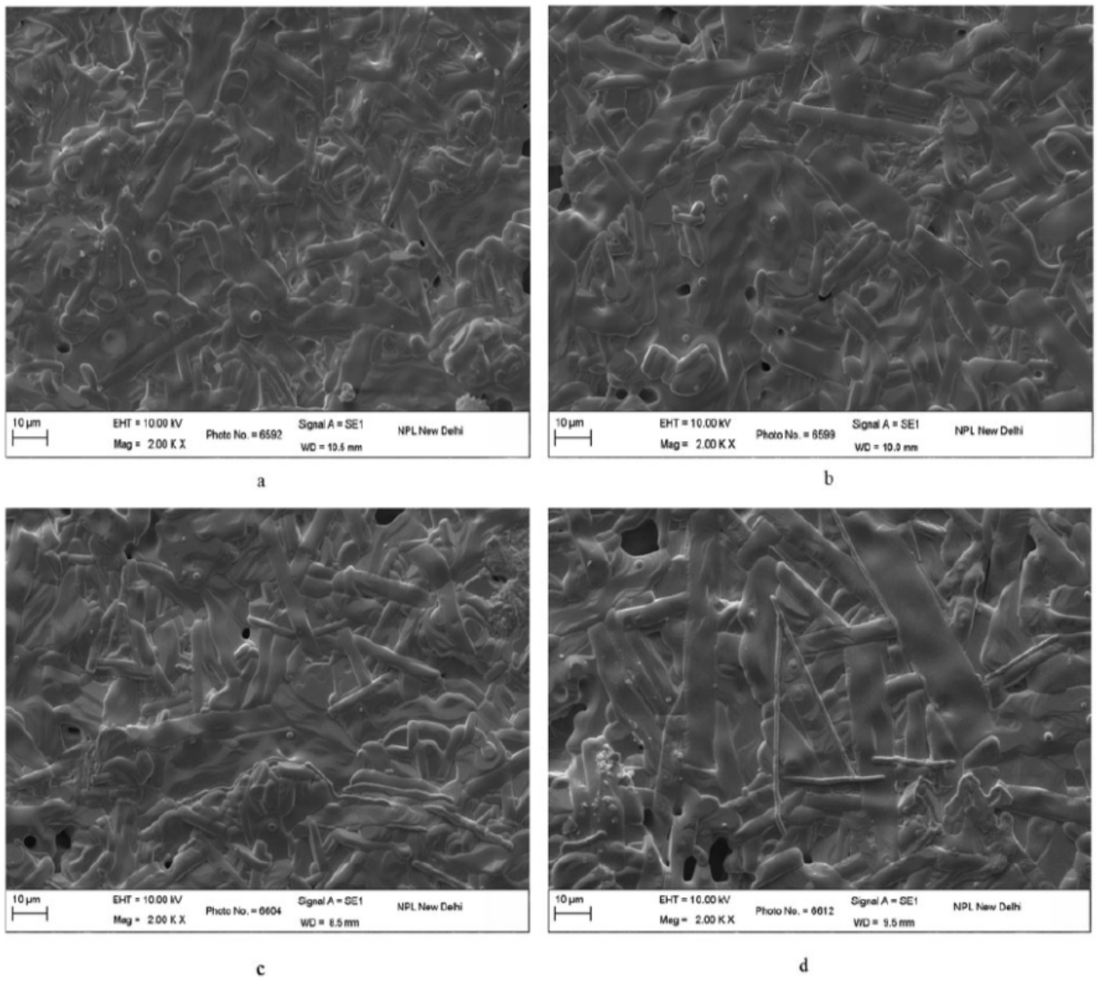

Fig. 4. SEM images of $YBa_2Cu_{3-x}Zn_xO_{7-\delta}$, (**a**) x = 0.01, (**b**) x = 0.03, (**c**) x = 0.05 and (**d**) x = 0.10 [Ref. 30].

C. $(Bi, Pb)_2Sr_2Ca_{n-1}Cu_nOy$

Bismuth based superconducting cuprates (in short named as BSCCO) is an another family of cuprate HTSc which are expressed by a general formula of $(Bi, Pb)_2Sr_2Ca_{n-1}Cu_nOy$. For ($n$ = 1, 2, 3), these are abbreviated as Bi2201, Bi2212 and Bi2223 phases, whose superconducting transition temperatures (T_c) are around 20, 85 and 110 K respectively [32]. Though the mechanism of superconductivity in HTSc superconductors has been extensively studied, it is still unclear. As a result of substitution experiments it is well known, that in HTSc's, there is a strong relationship between carrier concentration and transition temperature. In addition, intergrain carrier transportation is also a key factor in deciding the sharpness of the transition. It is a well known fact that intergrain region behaves as a non-conducting region. Thus grain connectivity becomes more important for the sharpness of transition and other critical parameters. The grain growth and its shape varies in $Bi_{2-x}Pb_xSr_2CaCu_2O_8$ (see Fig. 5) with substitution of Pb at Bi site ($0< x < 0.40$) [19]. From the flake type grain shape in pristine samples to needle type grain shape in x = 0.40 composition is observed from SEM micrographs. Moreover, improvement in the packing fraction and hence the inter-granular

connectivity was seen in the samples for x = 0.0 up to x = 0.16, which degrades with further increase in x. Decrease in the grain alignment with increase in Pb content has also been seen in SEM micrographs.

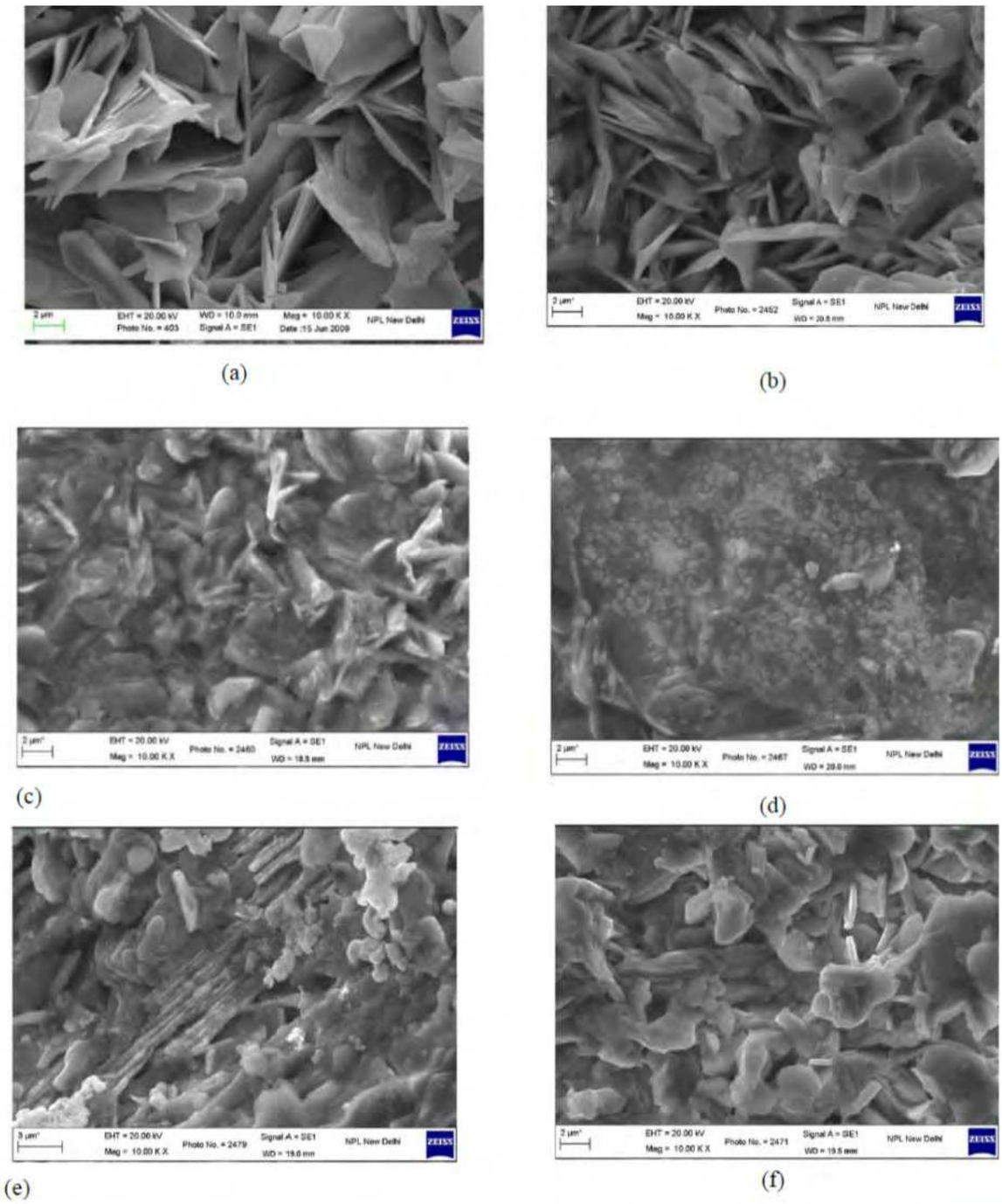

Fig. 5. SEM micrographs of $Bi_{2-x}Pb_x$ $Sr_2CaCu_2O_{8+\delta}$ (**a**) x = 0.04, (**b**) x = 0.06, (**c**) x = 0.08 and (**d**) x = 0.16 (**e**) x = 0.20 and (**f**) x = 0.40[Ref. 19].

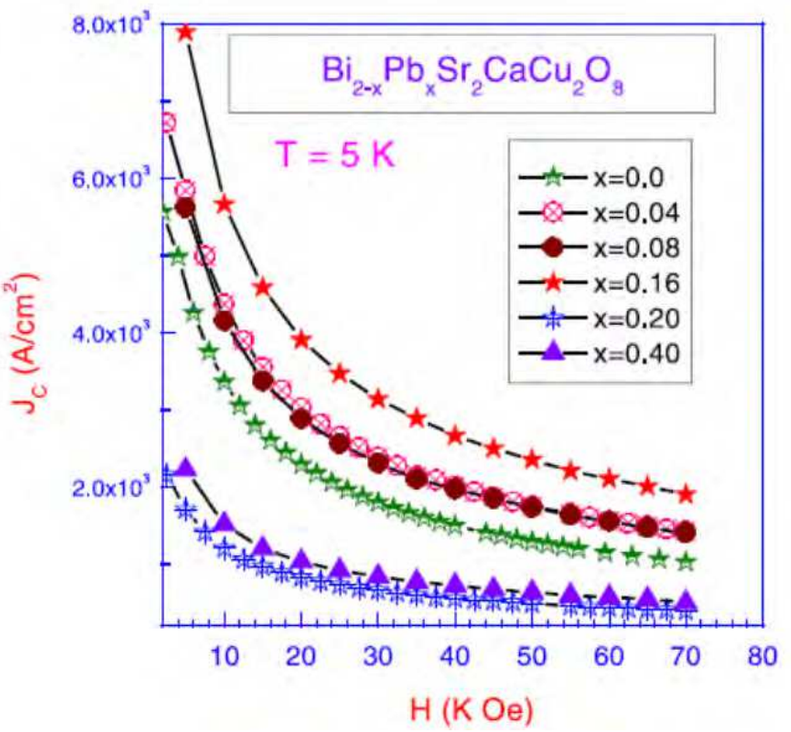

Fig. 6. *J*c measurements for $Bi_{2-x}Pb_x Sr_2CaCu_2O_{8+\delta}$ (x = 0 to 0.40) [Ref. 19].

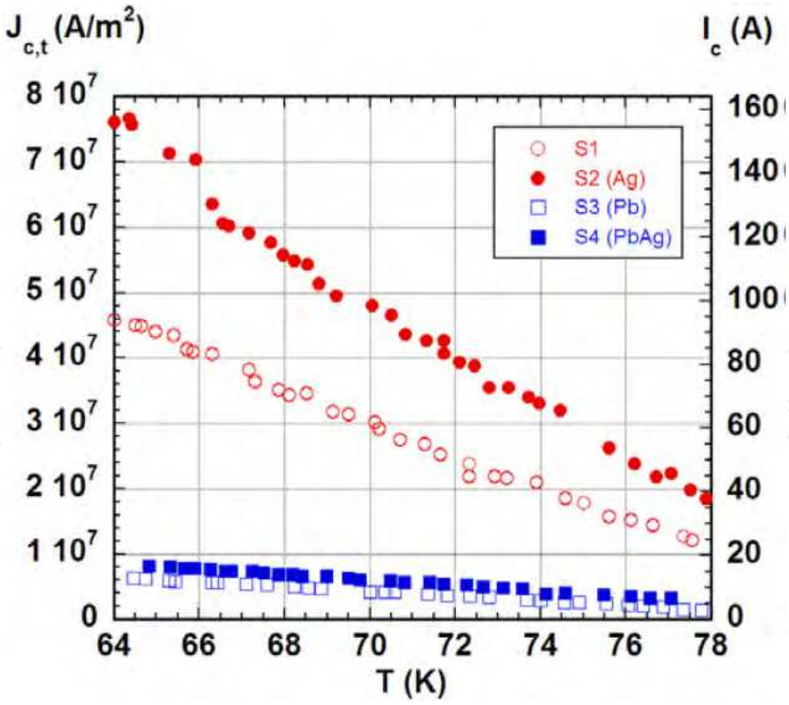

Fig. 7. Temperature dependence of the transport critical current densities, between 65 and 77 K and self-field, for the four samples.
Reprinted with permission from [Supercond. Sci. Technol. 22 (2009) 034012].

The critical current density data (see Fig. 6) for the same samples shows an increase in the current density with Pb substitution in pristine sample till x=0.16 after which it decreases with further increase in x. The decrease in conductivity for samples having $x > 0.16$ has been explained on the basis of the effects arising from decrease of the grain alignment, increase of porosity and secondary phases.

Also, A. Sotelo et al. [20] have studied the Lead (Pb) and Silver (Ag) doping of Bi-2212 samples. It was found that Pb doping results in the decrease of the transport critical current density (see Fig. 7), *Jc,t* (from 4.4 × 107 to 6 × 106 Am−2 at 65 K and self-field) as well as in the worsening of the mechanical properties, by about 35% compared to the undoped samples. In contrast, Ag doping results in the improvement of both the critical current density and mechanical strength.

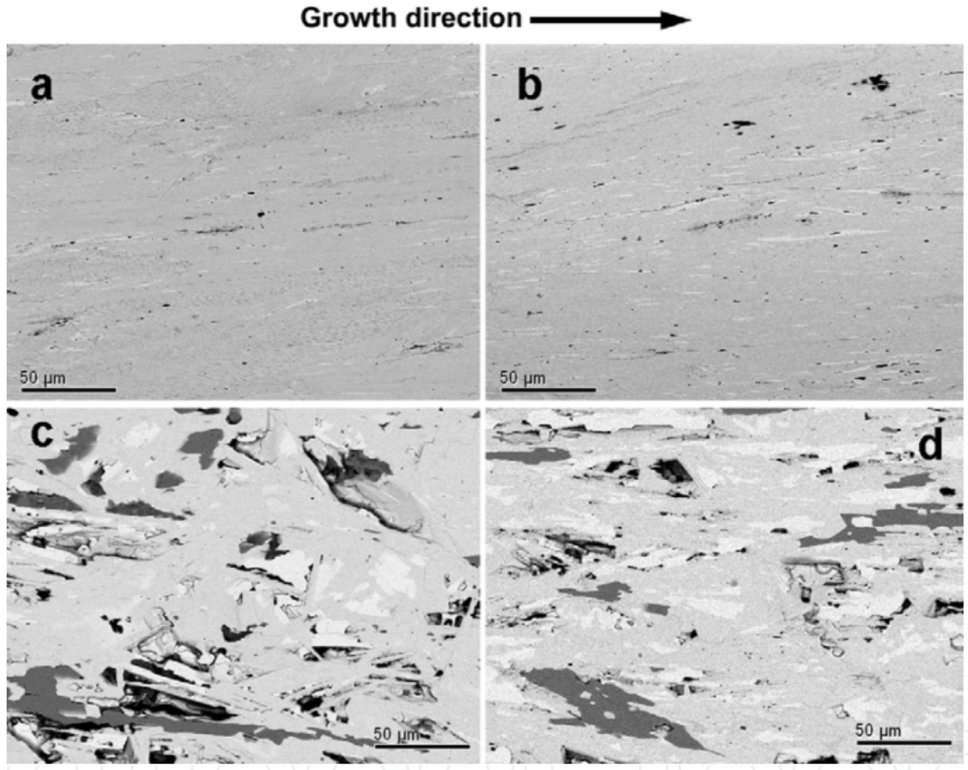

Fig. 8. Longitudinal SEM images obtained on annealed polished samples. (a) S1; (b) S2 (Ag); (c) S3 (Pb); and (d) S4 (PbAg). Phases can be identified as Bi-2201 (white contrast), Bi-free phases (dark grey; CuO, $Sr_{14}Cu_{24}O_{41}$, and $SrCuO_2$), plumbate-like phases and Bi-2212 (grey contrast), Ag (light grey contrast).
Reprinted with permission from [Supercond. Sci. Technol. 22 (2009) 034012].

These described effects are related to the microstructural observations (see Fig. 8) as, Pb doping dramatically reduces the texture, while Ag doping improves it. Moreover, for samples with Ag addition, an intergrowth of Bi-2223 inside the Bi-2212 grains is observed, which would explain the improved superconducting properties of these samples. The stability of these superconductors has been studied through the corrosion process in a moisture atmosphere [33]. By means of optical and SEM observations, several morphologies of the alteration products have been observed.

3.2 Flux pinning in MgB_2

Although cuprate superconductors exhibit very high transition temperatures, their in-field performance [34] is compromised by their large anisotropy, the result of which is to restrict high bulk current densities. On the other hand in-field performance (higher *Jc*), leads diboride of magnesium to much better candidate for application purposes besides its lower T_c than cuprates. With the magneto-optical (MO) and polarized light (PL), SEM was used to assess the issue of inhomogeneous and granular behaviour in MgB_2 [35]. It was speculated through SEM that the strongly shielding high-*Jc* regions are microstructurally subdivided on a scale of 100 nm. Also, in a darker central area a fine mixture of MgB_2 and a boron-rich phase was found through SEM [Fig. 9]. They concluded that the strongly shielding regions contain a large number of high-angle grain boundaries. Thus along with MO and PL, SEM suggests that MgB_2 is more similar to a low-*Tc* metallic superconductor than to a high-*Tc* copper oxide superconductor [35]. A sol-Gel synthesis of MgB_2 nanowires is reported Nath et.al [36]. SEM study reveals formation of a thick mesh of nanowires. The nanowires are found to be ca. 50–100 nm in diameter with very smooth surfaces having lengths up to at least 20 micrometer. It is observed that nanowires oriented vertically with respect to the electron beam. Thus SEM also revealed a hexagonal cross section for MgB_2 nanowires which is consistent with a degree of crystallinity. The Crystallinity of MgB_2 nanowires was also supported by their selected area electron diffraction (*SAED*) study on some individual nanowires. As MgB_2 has better candidature for practical applications various dopants has been added to improve its performance [6-14]. Arpita et al. [7] noted that with n-SiC addition though *Tc* decreases, but critical current density (*Jc*) and flux pinning improved significantly. Presence of Mg_2Si phase was also revealed through SEM and EDS [Fig. 10]. Dual reaction occurs with n-SiC addition first n-SiC reacts with Mg forming Mg_2Si and then free C is incorporated into MgB_2 at B site [37]. Thus both reactions help in the pinning of vortices which results in improved superconducting performance. Mg_2Si and excess carbon can be embedded within MgB_2 grains as nanoinclusions. They argued that due to the substitution of C at the B site the formation of a nanodomain structure takes place due to the variation of Mg-B spacing. These nanodomain defects, having the size of 2-3 nm, can also behave as effective pinning centers. So, highly dispersed nanoinclusions within the grains and the presence of nanodomain defects act as pinning centers and thus result in the improved *Jc(H)* behavior for the n-SiC doped samples.

3.3 Pnictides: Chemical composition and electrical transport

A. $REFeAsO_{1-x}F_x$ (1111)

Iron pnictides are the latest entrant in family of high temperature superconductors [38]. Superconductivity originates in parent pnictides *RE*FeAsO with doping of F at O site. The reactive nature of *REs* towards oxygen results a very critical synthesis condition for these compounds. Though the compounds are being synthesized in inert/oxygen controlled atmosphere, it is very hard to acquire the desired composition. Thus it is better to analyze the chemical composition of the synthesized compound before going insight and describing the physical properties. Thus *SEM* with *EDS* can be very useful in invoking the composition (especially effective F concentration) of the arsenides. The *SEM* analysis of the parent and non superconducting SmFeAsO compound after metallographic preparation reveals very small amounts of unreacted phases (iron arsenides), which are completely dissolved after

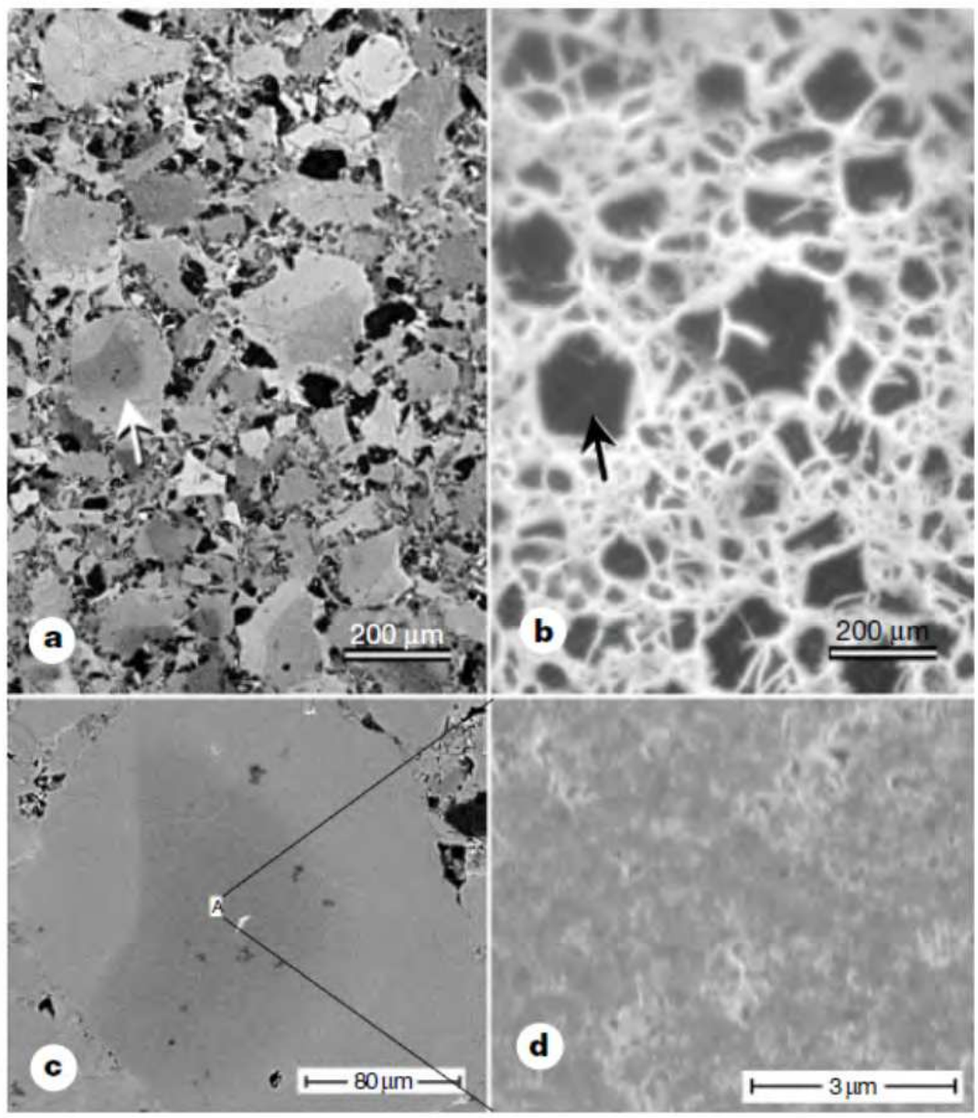

Fig. 9. Polarized light microscope and magneto-optical images of the same area of sample B are compared in (**a)** and (**b)**, respectively. Bright regions of (**b)** indicate areas where magnetic flux has penetrated the sample after a field of 120 mT was applied after cooling the sample in zero field to 11 K. Image (**c)** presents a magnified view using SEM backscattered electron imaging of the strongly superconducting region marked with an arrow in (**a)** and (**b)**. At higher resolution, image **(d)**, a secondary electron examination of the central region in (**c)**, reveals that the area marked by an arrow in (**a)** and (**b)** has, 100-nm, fine-scale structure
[Reprinted by permission from Macmillan Publishers Ltd: NATURE 410 (2001) 186].

sintering. In general, sintering greatly increases the density of the samples, but favours the formation of Sm_2O_3 small particles. This feature reveals that at the sintering temperature the formation of Sm_2O_3 competes with the thermodynamic stability of the oxy-pnictide. S. Kaciulis et al. [39] studied $SmFeAsO_{0.85}F_{0.15}$ sample with *SEM*, *EDS* and *XPS*. *SEM* image after the fracture manifests the crystals appear clean at the surface, without any contamination of

secondary phases. On the other hand another *SEM* image of the same sample after metallographic preparation reveals that crystals are aggregated within a matrix constituted of FeAs, which was also evidenced by their *EDS* analysis. However, their XPS study speculated that the formation of secondary phases, such as FeAs and SmOF. The discrepancy with EDS data, indicating only the presence of FeAs in the matrix, was explained by different analysis depth: up to a few micrometers for *EDS* and only a few nanometers for *XPS*. However, the aggregation of $REFeAsO_{0.85}$ crystals in FeAs matrix is also observed in Back Scattered *SEM* study [Fig. 11] of Ketnami et al. [40]. The absence of significant transport currents in polycrystalline samples has raised the concern that there is a significant depression of the superconducting order parameter at grain boundaries (GB) [41-43]. Remnant magnetization and *MO* studies of polycrystalline $NdFeAsO_{0.85}$ and $SmFeAsO_{0.85}$ uncovered that intergrain and intra-grain current densities had different temperature dependences and differed by three orders of magnitude, leaving open the possibility of an intrinsic GB blocking effect [40]. Moreover, the BSE-SEM images revealed that even the best $SmFeAsO_{0.85}$ bulk had non-superconducting Fe-As and RE_2O_3 occupying at least three quarters of the $REFeAsO_{0.85}$ GBs, making the active current path certainly much smaller than the geometrical cross-section of the sample [40]. Further to reveal the active local current paths, combined low temperature laser scanning microscopy (LTLSM) and SEM studies had been made [44]. With the *SEM* images they are able to show significant micro-structural differences between various regions of the sample. It is revealed that insulating Sm_2O_3 has a small surface to volume ratio and is mostly located within $SmFeAsO_{0.85}$ grains, so it has the smallest effect on current transport. On the other hand the dark gray Fe-As phase wets many GBs, thus interrupting grain to grain supercurrent paths, which are further degraded by extensive cracking, sometimes at GBs.

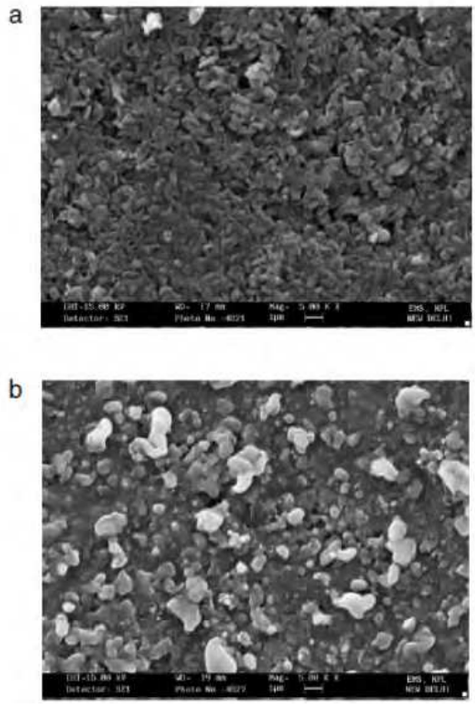

Fig. 10. (a), (b) SEM images of pure MgB_2 and 10 wt%n-SiC added samples.
Reprinted with permission from [Nanotechnology 19 (2008) 125708]

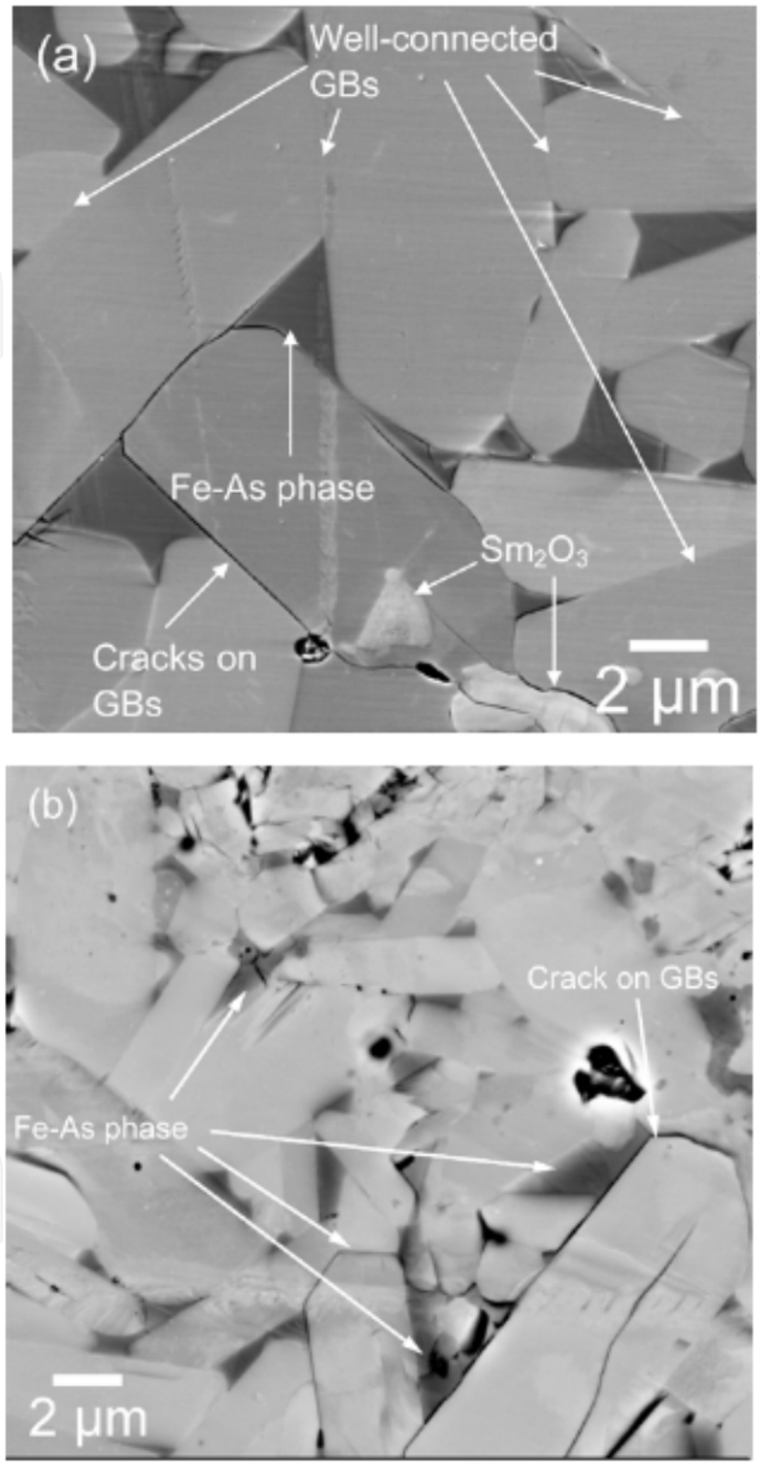

Fig. 11. BSE image of the (a) Sm and (b) Nd sample at high magnification. Although some grain boundaries are well connected, others are clearly obstructed by the Fe-As phase (dark contrast), Sm_2O_3 or Nd_2O_3 (white contrast) and cracks.
Reprinted with permission from [Supercond. Sci. Technol. 22 (2009) 015010].

Also, magnetic contamination is detected through *SEM* in the case of NdFeAsO single crystals grown out of NaAs flux under ambient pressure [45]. It is observed that some crystals show a lambda anomaly in the specific heat curve at ~12 K while the same is absent in others. They examined the cleaved (001) surfaces with *SEM* which were showing lambda anomaly. They turned to look at the edges of the crystals carefully. A 10-μm-thick layer was observed on the edges of the NdFeAsO crystals. With *EDS* it was found that some particles of TaAs, were surrounded by some very fine particles. After removal of that impurity the lambda anomaly disappeared. Thus with the help of *SEM* and *EDS* we can find out the actual cause which leads particular nature of a material.

B. Ba/Sr/K/Fe_2As_2 (122)

Soon after the discovery of 1111 family, other superconducting families based on FeAs layers (122, 111 and 11 structure) were reported, such as (Ba,K)Fe_2As_2 [46], LiFeAs [47], and FeSe [48]. Among all of these iron-based superconductors, the 122-type superconductors with a *T*c of 38 K have a lower synthesis temperature and are oxygen free in comparison to the 1111-type. In addition, its *T*c is much higher than those of the 111 and 11-type superconductors. SEM is used ingeniously to study the single crystal of Ba(Fe/Co)$_2As_2$ [16]. The topographic images of cleaved surface of optimally doped $BaFe_{1.8}Co_{0.2}As_2$ with *uniform* contrast have been observed in the secondary electron emission images acquired by SEM. They used secondary electron emission mode as it can register the contrast according to topography, chemical composition, and surface barrier (work function or ionization energy) of the sample [49] Small darker regions in the SEM image have been identified as marked by a rectangular box in Fig 12 (a). An SEM zoom-in image in the dark region reveals microscopic *domain* structures [Fig. 12]. They made resolved electrical transport measurements with use of SEM which have provided direct evidence of the coupling between superconductivity and local environment that is reflected by Co-concentration variation. In the uniform regions, the superconducting transition occurs at T_C = 22.1 K for 10% fixed percentage of the normal-state resistance. In the domain regions, although the onset superconducting transition temperature is found very close to that of the uniform regions, T_C varied over a broader range of 0.3-3.2 K. In addition, resistance of the domain regions above the transition onset temperature was noticed higher than that of the uniform region, indicating higher defect density in the domain regions.

Like HTSc's improvement in J_c is observed with increase of grain size in 122 systems also [50]. Effect of sintering temperature on the microstructure and superconducting properties of $Sr_{0.6}K_{0.4}Fe_2As_2$ bulk samples was made. It was found that the annealing temperature had little influence on the critical temperature *T*c. However, the irreversibility field H_{irr} and J_c were significantly affected by the sintering temperature. The *SEM* images reveal although samples had similar microstructure, the grain size increases monotonically as the sintering temperature rises. The grain size was less influenced by temperatures over 850 C. It was concluded the J_c enhancement may result mainly from better grain connectivity due to the decrease of impurity phases.

4. Limitations

Although SEM is very useful in finding grain size, their connectivity and then revealing various microscopic properties with physics behind that but there are some limiting

conditions for it. It is not a complete characterization in the sense that it needs extra characterization techniques such as TEM, PL, XPS and MO to support the results. The sensitivity of SEM is known to be relatively poor for lighter elements such as B, C and O. Thus through EDS results, the actual percentage ratio cannot be determined as very light elements boron and carbon are lesser sensitive in comparison to others elements [15]. In nano-TiO_2 doped samples [51] almost similar micrographs for all samples was found irrespective of whether they are doped with n-TiO_2 or not. In their study with HRTEM it was concluded that several black holes that appear in the image are presumably the n-TiO_2.

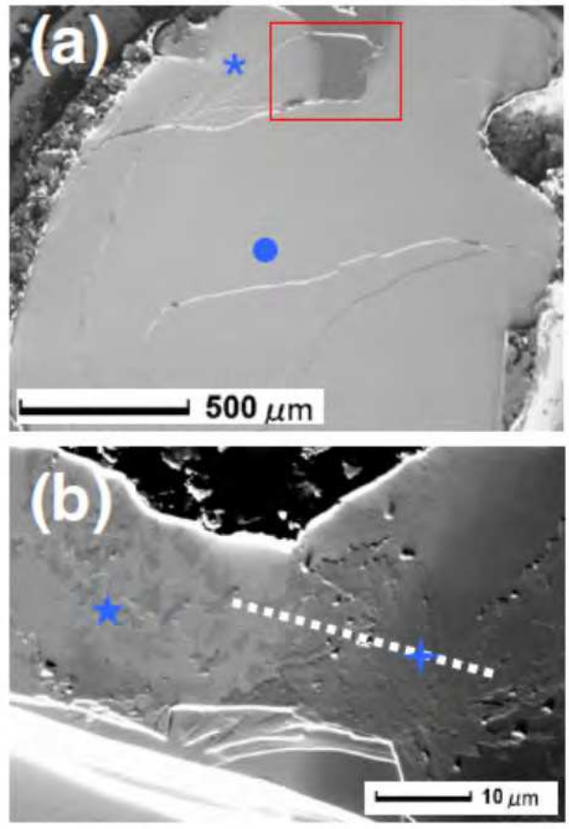

Fig. 12. Topographic images of cleaved surfaces of $BaFe_{1.8}Co_{0.2}As_2$ single crystal. (a) SEM image showing uniform contrast with some dark regions near the edge of crystal, as marked by a rectangular box. (b) Zoom-in SEM image showing domain structures. Marked regions by symbols and a dash line in (a) and (b) indicate where the transport measurements and composition probing are carried out.
Reprinted (Fig.) with permission from [T.-H. Kim, R. Jin, L. R. Walker, J. Y. Howe, M. H. Pan, J. F. Wendelken, J. R. Thompson, A. S. Sefat, M. A.McGuire, B. C. Sales, D. Mandrus, A. P. Li, Phys. Rev. B 80 (2009) 214518].

5. Summary

Summarily we can see that *SEM* has been widely used to explore the superconducting behavior. Grain size matters a lot in deciding the superconducting parameters of cuprate

HTSc. Some of the important aspects with which *SEM* deals with, is the grain size, morphology and alignment, structural defects, chemical composition. It has been used widely to explore from HTSc's, diborides to pnictides. With the time ways to use *SEM* and to extract information from superconductors got improved. Earlier for HTSc's it was used simply in finding grain size, grain connectivity and to figure out impurity regions. With these parameters superconducting behaviour was explained. Along with this in diborides it was also used to figure out the pinning centers and hence to enhance the applicable parameters. In Pnictides with spatially resolved electrical transport measurements it provided direct evidence of the coupling between superconductivity and local environment variation. We suppose in future SEM will be more plausible to understand so that superconductivity is better understood and improved.

6. Acknowledgements

Author S. K. Singh would like to acknowledge *CSIR*, India for providing fellowships. We are very much thankful NPG [Macmillan Publishers Ltd: NATURE 410 (2001) 186], IOP Publishing Ltd.{(SUST [Supercond. Sci. Technol. 22 (2009) 015010, Supercond. Sci. Technol. 22 (2009) 034012] and Nanotechnology **19** (2008) 125708)}, and APS [Phys. Rev. B 80 (2009) 214518] for providing permissions for the reprints of the images. We want to acknowledge the authors of the Ref. No. [15], [16], [20], [35], [40] for giving their consent to re-use the images.

7. References

[1] J. W Ekin, Adv. Ceram. Matter. 2 (1987) 586
[2] A Rosko, Y. M Chiang, J. S Moodera and D. A Rudman, American Ceram. Socie. (1988) 308
[3] D. S smith, S. Suasmoro, C.Gault, F. Caillaud and A. Smith, Revue Phys. Appl. 25 (1990) 61
[4] http://www.astm.org/
[5] http://www.astm.org/Standards/E112.htm
[6] T. Nagano, Y. Tomioka, Y. Nakayama, K. Kishio, K. Kitazawa, Phys. Rev. B 48 (1993) 9689
[7] S X Dou *et al.* Appl. Phys. Lett. 81 (2002) 3419
[8] W. K. Yeoh *et al.* Supercond. Sci. Technol. 19 (2006) 596
[9] H. Yamada, *et al.* Supercond. Sci. Technol. 19 (2006) 175
[10] C H Cheng, *et al.* Supercond. Sci. Technol. 16 (2003) 1182
[11] Senkowicz *et al.* Appl. Phys. Lett. 86 (2005) 202502
[12] R H T Wilke, *et al.* Phys. Rev. Lett. 92 (2004) 217003
[13] Xiang *et al.* Physica C 386 (2003) 611
[14] A. Matsumoto, *et al.* Supercond. Sci. Technol. 16 (2003) 926
[15] Arpita Vajpayee, V P S Awana, G L Bhalla and H Kishan Nanotechnology 19 (2008) 125708
[16] T.-H. Kim, R. Jin, L. R. Walker, J. Y. Howe, M. H. Pan, J. F. Wendelken, J. R. Thompson, A. S. Sefat, M. A. McGuire, B. C. Sales, D. Mandrus, A. P. Li, Phys. Rev. B 80 (2009) 214518
[17] Charles P. Poole, Jr., Handbook of superconductivity, Academic Press, California (2000)
[18] D. Sharma, Ranjan Kumar, H. Kishan and V.P.S. Awana, J Supercond Nov Magn 24 (2011) 205
[19] J. Kumar *et al.* J Supercond Nov Magn 23(2010) 493
[20] A Sotelo *et al.* Supercond. Sci. Technol. 22 (2009) 034012

[21] J.C. Bednorz and K.A. Müller, Zeitschrift für Physik B. 64(2) (1986) 189
[22] Chiang, Y.-M., Rudman, D.A., Leung, D.K., Ikeda, J.A.S., Roshko, A., Fabes, B.D., Physica C 152 (1988) 77
[23] J.W. Ekin *et al.* J. Appl. Phys. 62, (1987) 4821
[24] Shiming Zhou, Jiyin Zhao, Songnan Chu, Lei Shi Physica C 451 (2007) 38.
[25] R.J. Cava, Science 247 (1990) 656
[26] R. Gagnon, C. Lupien, and L. Taillefer, Phys. Rev. B 50 (1994) 3458
[27] M. Karppinen, V.P.S. Awana, Y. Morita, H. Yamauchi, Physica B, 312 (2003) 62
[28] P.R. Slater, C. Greaves: Physica C 180 (1991) 299
[29] Shiva Kumar, Anjana Dogra, M. Husain, H. Kishan and V.P.S. Awana, J. Alloys and compd. 352 (2010) 493
[30] N.P Liyanawaduge, Shiva Kumar Singh, Anuj kumar, V.P.S Awana and H.Kishan, J Sup. and Novel Magn doi: 10.1007/s10948-010-1063-7
[31] X.S. Wu, W.S. Tan, Y.M. Xu, E.M. Zhang,J. Du, A. Hu, S.S. Jiang, J. Gao Physica C 398 (2003) 131
[32] J. M. Tarascon *et al.* Phys. Rev. B 38 (1988) 8885
[33] O. Monnereau, Z.C. Kang, E. Russ, I. Suliga, G. Vacquier, T. Badéche, C. Boulesteix, A. Casalot Applied Superconductivity April (1995) 197
[34] Yeshurun, Y., Malozemoff, A. P. & Shaulov, A. Magnetic relaxation in high-temperature superconductors. Rev. Mod. Phys. 68 (1996) 911
[35] L. D. Larbalestier *et al.* NATURE 410 (2001) 186
[36] Manashi Nath and B. A. Parkinson Adv. Mater. 18 (2006) 1865
[37] S X Dou *et al.* Phys. Rev. Lett. 98 (2007) 097002
[38] Y. Kamihara, T. Watanabe, M. Hirano, H. Hosono, J. Am. Chem. Soc. 130 (2008) 3296
[39] S. Kaciulis *et al.* Surf. Interface Anal. 42 (2010) 692.
[40] F. Kametani, A. A. Polyanskii, A. Yamamoto, J. Jiang, E. E. Hellstrom, A. Gurevich, D. C. Larbalestier, Z. A. Ren, J. Yang, X. L. Dong, W. Lu, and Z. X. Zhao, Supercond. Sci. Technol. 22 (2009) 015010.
[41] A. Yamamoto, J. Jiang, C. Tarantini, N. Craig, A. A. Polyanskii, F. Kametani,F. Hunte, J. Jaroszynski, E. E. Hellstrom, D. C. Larbalestier, R.Jin, A. S. Sefat, M. A. McGuire, B. C. Sales, D. K. Christen, and D. Mandrus, Appl. Phys. Lett. 92 (2008) 252501
[42] B. Senatore, G. Wu, R. H. Liu, X. H. Chen, and R. Flukiger, Phys. Rev. B 78 (2008) 054514
[43] R. Prozorov, M. E. Tillman, E. D. Mun, and P. C. Canfield, New J. Phys.11 (2009) 035004
[44] F. Kametani, P. Li,1 D. Abraimov, A. A. Polyanskii, A. Yamamoto, J. Jiang, E. E. Hellstrom, A. Gurevich, D. C. Larbalestier, Z. A. Ren, J. Yang, X. L. Dong, W. Lu, and Z. X. Zhao Appl. Phys. Lett. 95 (2009) 142502
[45] J.-Q. Yan, Q. Xing, B. Jensen, H. Xu, K. W. Dennis, R. W. McCallum, and T. A. Lograsso Phys. Rev. B. 84 1250
[46] M. Rotter, *et al.* Phys. Rev. B 78 (2008) 020503
[47] X C Wang, *et al.* Solid State. Commun. 148 (2008) 538
[48] Hsu F C *et al.* Proc. Natl Acad. Sci. USA 105 (2008) 14262
[49] Ma Y W, Gao Z S, Wang L, Qi Y P, Wang D L and Zhang X P Chin. Phys. Lett. 26 (2009) 037401
[50] Zhiyu Zhang, Yanpeng Qi, Lei Wang, Zhaoshun Gao, DongliangWang, Xianping Zhang and Yanwei Ma Supercond. Sci. Technol. 23 (2010) 065009
[51] H. Kishan, V.P.S. Awana, T.M. de Oliveira, Sher Alam, M. Saito, O.F. de Lima Physica C 458 (2007) 1

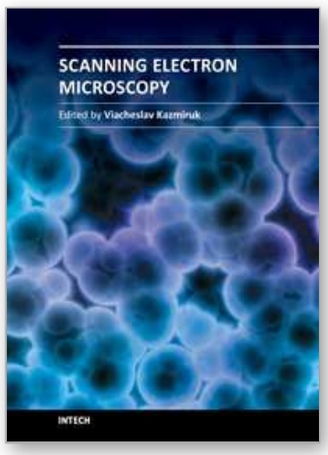

Scanning Electron Microscopy
Edited by Dr. Viacheslav Kazmiruk

ISBN 978-953-51-0092-8
Hard cover, 830 pages
Publisher InTech
Published online 09, March, 2012
Published in print edition March, 2012

Today, an individual would be hard-pressed to find any science field that does not employ methods and instruments based on the use of fine focused electron and ion beams. Well instrumented and supplemented with advanced methods and techniques, SEMs provide possibilities not only of surface imaging but quantitative measurement of object topologies, local electrophysical characteristics of semiconductor structures and performing elemental analysis. Moreover, a fine focused e-beam is widely used for the creation of micro and nanostructures. The book's approach covers both theoretical and practical issues related to scanning electron microscopy. The book has 41 chapters, divided into six sections: Instrumentation, Methodology, Biology, Medicine, Material Science, Nanostructured Materials for Electronic Industry, Thin Films, Membranes, Ceramic, Geoscience, and Mineralogy. Each chapter, written by different authors, is a complete work which presupposes that readers have some background knowledge on the subject.

InTech Europe
University Campus STeP Ri
Slavka Krautzeka 83/A
51000 Rijeka, Croatia
Phone: +385 (51) 770 447
Fax: +385 (51) 686 166
www.intechopen.com

InTech China
Unit 405, Office Block, Hotel Equatorial Shanghai
No.65, Yan An Road (West), Shanghai, 200040, China
中国上海市延安西路65号上海国际贵都大饭店办公楼405单元
Phone: +86-21-62489820
Fax: +86-21-62489821

IntechOpen